Honors Undergraduate Theses   UCF Theses and Dissertations

2017

Power Distribution of Terahertz Emission from Hexagonal BSCCO Microstrip Antennas

Andrew E. Davis
University of Central Florida

POWER DISTRIBUTION OF TERAHERTZ EMISSION FROM HEXAGONAL BSCCO MICROSTRIP ANTENNAS

by

ANDREW DAVIS

A thesis submitted in partial fulfilment of the requirements
for the Honors in the Major Program in Physics
in the College of Sciences
and in the Burnett Honors College
at the University of Central Florida
Orlando, Florida

Fall Term, 2017

Thesis Chair: Dr. Richard Klemm

ABSTRACT

We analyze the distribution of coherent terahertz radiation from a regular hexagonal microstrip antenna (MSA) made from the high-T_c superconductor $Bi_2Sr_2CaCu_2O_{8+\delta}$ (BSCCO). We discuss the C_{6v} symmetry of the solutions of the wave equation on a hexagonal domain and distinguish between the closed-form and non-closed-form solutions. The closed-form wavefunctions of the transverse magnetic (TM) electromagnetic cavity modes are presented and formulas for the radiated power arising from the uniform part of the AC Josephson current and from the resonant cavity modes are derived. The wavefunctions and angular distribution of radiation from both sources are plotted for sixteen of the lowest-energy modes. Finally, we comment on the relevance of these power distributions to hexagonal arrays of equilateral triangular MSAs and propose a strategy for studying the non-closed-form modes.

ACKNOWLEDGMENTS

TABLE OF CONTENTS

LIST OF FIGURES

LIST OF TABLES

CHAPTER 1: INTRODUCTION

Several candidates have been proposed as possible sources of coherent electromagnetic radiation in the terahertz (THz) frequency range (between 0.3 and 3 THz) [1]. Improvements in resonant tunneling diodes [2] and quantum cascade lasers [3] have partially filled this gap, but solid-state technologies capable of producing coherent, continuous radiation at sufficiently high powers for applications with the frequency range known as the *terahertz gap* (0.5 to 1.3 Thz) have continued to elude researchers. Such sources of THz radiation would have applications in any field that employs spectroscopy, such as medicine, biology, security, and communications [4]. One promising category of candidates for filling the terahertz gap is superconductor-based devices.

The physical mechanism by which these superconducting sources of radiation operate is the Josephson effect, a quantum mechanical phenomenon attributable to the coherence of the superconducting state [5]. The effect occurs within a Josephson junction, i.e., a pair of weakly coupled superconducting electrodes, and involves the conversion of a DC bias voltage to a high-frequency superconducting AC current across the junction. A useful consequence of the Josephson effect is that the frequency of the emitted radiation should be tunable, since it can be controlled by manipulating the DC bias voltage across the junction. The frequency of the AC supercurrent is directly proportional to the applied DC voltage V_{DC} and is given by the Josephson relation for a single junction

$$f = \frac{2\pi}{\Phi_0} V_{DC} \tag{1.1}$$

where $\Phi_0 = h/(2e)$ is the magnetic flux quantum (2.07×19^{-15} Wb).

Josephson junctions may be created artificially or they may be intrinsic to the crystal structure of a superconductor. The high-T_c layered superconductor $Bi_2Sr_2CaCu_2O_{8+\delta}$ (BSCCO) consists

1

of alternating insulating layers of Bi–Sr–O and superconducting layers of CuO_2 [6]. The copper oxide layers are weakly coupled and therefore the crystal behaves as a densely packed stack of intrinsic Josephson junctions (IJJs). Another well-known high-T_c layered superconductor, famous for being the first superconductor discovered with a critical temperature exceeding the boiling point of nitrogen, is $YBa_2Cu_3O_7$ (YBCO), but YBCO is not a suitable candidate for terahertz devices because the superconducting layers are too strongly coupled and the Josephson effect fails to occur [1].

Various devices have been fabricated that exploit the intrinsic Josephson junctions within a BSCCO mesa. Typically, a groove is inscribed (e.g., by focused ion beam milling or Ar ion milling) in a crystal of BSCCO, producing a mesa about 1 μm thick of any desired geometry attached to the superconducting substrate [7]. The mesas essentially function as microstrip antennas (MSAs) and can be analyzed with standard antenna theory. These earlier terahertz oscillators suffered from Joule self-heating effects, which led to the formation of local hot spots where the sample ceased to superconduct, limiting the efficiency of the devices. The mesas have been further improved by cleaving them from the substrate to produce stand-alone mesas, which are more easily thermally managed [8].

CHAPTER 2: LITERATURE REVIEW

Previous experiments have studied BSCCO mesas of various geometries, both stand-alone and attached to the superconducting substrate. In an early experiment [9], Ar ion milling was used to carve rectangular mesas from single crystals of BSCCO. Each mesa was approximately 1 μm thick (in the direction of the c-axis of the crystal), 300 μm long, and 60 μm wide, containing on the order of N 10^3 IJJs. The surface of the mesa was plated with Au and electrical leads were attached to the surface of the mesa and to the superconducting substrate. A DC voltage was applied across the mesa, triggering the emission of Josephson radiation with frequency given by the formula

$$\omega_J = \frac{2e}{\hbar} \frac{V_{DC}}{N} \tag{2.1}$$

.

When the DC voltage is varied, the frequency of the emitted radiation varies accordingly, but is greatly amplified at some frequencies. This can be explained [10] by modeling the mesa as a cavity in which electromagnetic waves propagate. These electromagnetic cavity modes are determined by the geometry of the cavity; in the rectangular case [7], their wavevectors are

$$k_{mp} = \pi \left[\left(\frac{m}{w} \right)^2 + \left(\frac{p}{\ell} \right)^2 \right]^{1/2} \tag{2.2}$$

where w and ℓ are the width and length of the cavity and m and p are integers. When the DC voltage is applied to the mesa, the resulting AC Josephson frequency or its higher harmonics ($n\nu_J$, where n is an integer, and $\nu_J = \omega_J/2\pi$) can lock onto these cavity modes and resonate. The radiation from these excited electromagnetic cavity modes is comparable in power to that produced by the AC

Josephson current (which is overlooked in the cavity model), amplifying the intensity of radiation at these frequencies [11].

The uniform part of the AC Josephson current through the mesa, combined with Ampère's Law, implies a nonzero $\boldsymbol{H}(\boldsymbol{x}', t)$ in the mesa. Since the AC Josephson current is not negligible compared to the cavity modes, it must be taken into consideration in the Ampère boundary condition. One way to treat the boundary condition is to employ Love's equivalence principles [12], which replace the electric field within the mesa by an equivalent surface magnetic current density source and the magnetic field by an equivalent surface current density source. This technique is applicable to mesas of any geometry and can be used to derive formulae for the angular dependence of the emitted radiation.

In addition to rectangular mesas, other geometries have also been studied experimentally [13] and theoretically [7], including cylindrical [16], equilateral triangular, acute isoceles triangular, right triangular, and square mesas, and the power distributions have been found analytically for the cylinder, square, and equilateral triangle geometries.

CHAPTER 3: MAIN FINDINGS

Solutions of the wave equation on a hexagonal domain

We begin by imposing a coordinate system on a hexagon of side length a, centering it at the origin, and labeling the vertices A through F. The hexagon lies in the xy-plane, and the Josephson current is therefore in the z-direction, perpendicular to the layers of BSCCO. The coordinate axes are oriented such that a pair of opposite sides ($\overline{AB}$ and $\overline{DE}$ in Fig. 2.1) of the hexagon are parallel to the y-axis.
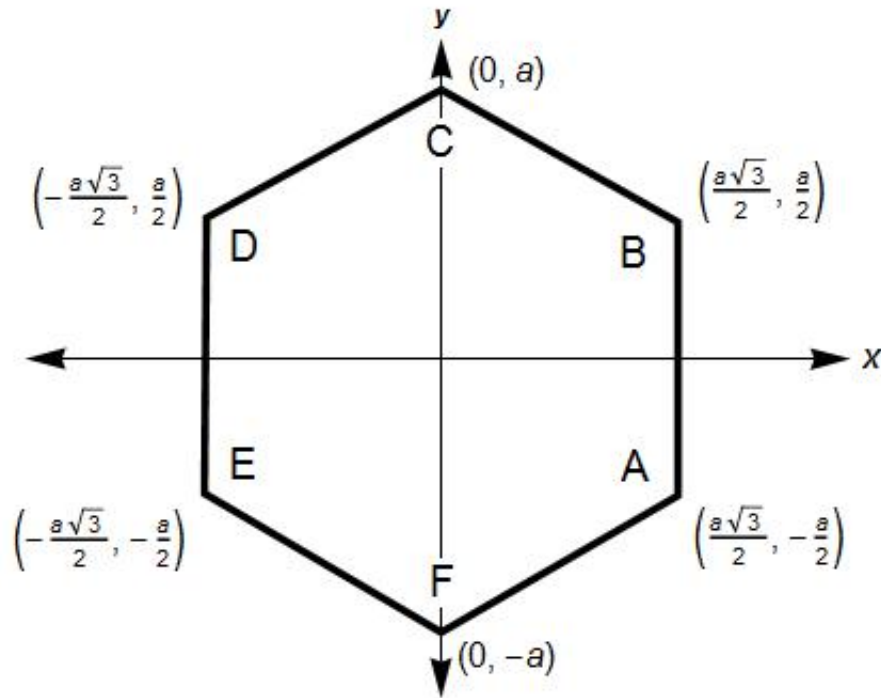
Figure 3.1: Hexagon of side length a centered at the origin with vertices labeled.

The wavefunction must satisfy the Helmholtz equation $\nabla^2 \Psi + k^2 \Psi = 0$ in addition to the relevant boundary conditions. In contrast to the case of the square, the rectangle, the equilateral triangle, etc., not all of the solutions of the wave equation on the hexagonal domain can be expressed in closed form; about half of them [17] can be written only as infinite series. Only the closed-form solutions are considered in this paper. Like the equilateral triangle, the solution of which was discovered by Lamé [18], the hexagon is an interesting case in which there exist closed-form solutions to the wave equation which cannot be found by ordinary separation of variables; rather, the full solution is the sum of three terms, each of which is a product of trigonometric functions exhibiting separation of variables. The forms of the closed-form solutions on the hexagon fall into two categories: the *even* forms $\Psi^e_{\ell mn}(x, y)$ and the *odd* forms $\Psi^o_{\ell mn}(x, y)$. They are given by

$$
\begin{aligned}
\Psi^e_{\ell mn} = & \cos\left[\frac{2\pi\ell}{a\sqrt{3}} x\right] \cos\left[\frac{2\pi(m-n)}{3a} y\right] \\
& + \cos\left[\frac{2\pi m}{a\sqrt{3}} x\right] \cos\left[\frac{2\pi(n-\ell)}{3a} y\right] \\
& + \cos\left[\frac{2\pi n}{a\sqrt{3}} x\right] \cos\left[\frac{2\pi(\ell-m)}{3a} y\right]
\end{aligned}
\tag{3.1}
$$

$$
\begin{aligned}
\Psi^o_{\ell mn} = & \cos\left[\frac{2\pi\ell}{a\sqrt{3}} x\right] \sin\left[\frac{2\pi(m-n)}{3a} y\right] \\
& + \cos\left[\frac{2\pi m}{a\sqrt{3}} x\right] \sin\left[\frac{2\pi(n-\ell)}{3a} y\right] \\
& + \cos\left[\frac{2\pi n}{a\sqrt{3}} x\right] \sin\left[\frac{2\pi(\ell-m)}{3a} y\right]
\end{aligned}
\tag{3.2}
$$

For the even forms, $\Psi^e_{\ell mn}(x, -y) = \Psi^e_{\ell mn}(x, y)$; that is, they are even under reflection over the x-axis (a consequence of the fact that cosine is an even function). Likewise, the odd forms satisfy

$\Psi^o_{\ell mn}(x, -y) = -\Psi^o_{\ell mn}(x, y)$, and they are odd under reflection over the y-axis (because sine is an odd function). These solutions satisfy both the wave equation and the requisite Neumann boundary condition—the tranverse magnetic boundary conditions demand that the normal derivative of the wavefunction vanish everywhere along the boundary of the hexagon. Note that if the Dirichlet boundary conditions were desired, so that the value of the wavefunction (not its derivative) vanished on the boundary, the cosine functions involving x could simply be replaced by sine functions, but these boundary conditions are not germane to our situation.

Although all three terms are required to satisfy the boundary conditions of the hexagon, each term individually constitutes a solution to the wave equation with the same wavevector k. Substituting each of these into the wave equation, we obtain three equations for k^2 in terms of the indices of the wavefunctions:

$$k^2 = \begin{cases} \dfrac{4\pi^2}{9a^2}\left[3\ell^2 + (m-n)^2\right] \\ \dfrac{4\pi^2}{9a^2}\left[3m^2 + (n-\ell)^2\right] \\ \dfrac{4\pi^2}{9a^2}\left[3n^2 + (\ell-m)^2\right] \end{cases} \tag{3.3}$$

Equating the last two of these expressions (in fact any pair will lead to the same result) gives the condition $(\ell + m + n)(m - n) = 0$. Either $m = n$ or $\ell = -m - n$, but the former case leads to $\ell = m = n$, which is redundant and yields no new eigenmodes, so we eliminate ℓ in favor of m and n and conclude that

$$k^2 = \frac{4\pi^2}{9a^2}\left[3\left(m+n\right)^2 + (m-n)^2\right] \implies k_{mn} = \frac{4\pi}{3n_r a}\sqrt{m^2 + mn + n^2} \tag{3.4}$$

where the index of refraction n_r has been inserted in the denominator to account for the properties

7

of the material (for BSCCO, $n_r \approx \sqrt{18} \approx 4.2$ in the pertinent frequency range). The even and odd wavefunctions now depend only on two indices, and they become

$$
\begin{aligned}
\Psi_{mn}^e = A_{mn}^e &\cos\left[\frac{2\pi(m+n)}{a\sqrt{3}}x\right]\cos\left[\frac{2\pi(m-n)}{3a}y\right] \\
&+ \cos\left[\frac{2\pi m}{a\sqrt{3}}x\right]\cos\left[\frac{2\pi(m+2n)}{3a}y\right] \\
&+ \cos\left[\frac{2\pi n}{a\sqrt{3}}x\right]\cos\left[\frac{2\pi(2m+n)}{3a}y\right]
\end{aligned}
\tag{3.5}
$$

$$
\begin{aligned}
\Psi_{mn}^o = A_{mn}^o &\cos\left[\frac{2\pi(m+n)}{a\sqrt{3}}x\right]\sin\left[\frac{2\pi(m-n)}{3a}y\right] \\
&+ \cos\left[\frac{2\pi m}{a\sqrt{3}}x\right]\sin\left[\frac{2\pi(m+2n)}{3a}y\right] \\
&- \cos\left[\frac{2\pi n}{a\sqrt{3}}x\right]\sin\left[\frac{2\pi(2m+n)}{3a}y\right]
\end{aligned}
\tag{3.6}
$$

where A_{mn}^e and A_{mn}^o are normalization constants chosen so that the integral of the square of the wavefunction over the entire hexagon equals unity. It can be shown that the values of these constants are

$$
|A_{mn}^e|^2 = \begin{cases}
\dfrac{2}{27\sqrt{3}\,a^2}, & m = n = 0; \\[2ex]
\dfrac{4}{9\sqrt{3}\,a^2}, & m > n = 0, n > m = 0, \text{ or } m = n; \\[2ex]
\dfrac{8}{9\sqrt{3}\,a^2}, & m, n > 0 \text{ and } m \neq n.
\end{cases}
\tag{3.7}
$$

8

and

$$|A^o_{mn}|^2 = \begin{cases} \dfrac{4}{9\sqrt{3}\,a^2}, & m > n = 0 \text{ or } n > m = 0; \\ \dfrac{8}{9\sqrt{3}\,a^2}, & m, n > 0 \text{ and } m \neq n. \end{cases} \qquad (3.8)$$

.

Observe, however, that the even $(0,0)$-mode is constant everywhere and has wavevector $k_{00} = 0$, corresponding to a wave with no energy, so this solution is not of any interest. Also, the odd modes for which $m = n$ are identically zero and therefore are not normalizable and do not radiate.

Symmetries of the wavefunctions

Table 3.1: C_{6v} Character Table

C_{6v}	E	$2C_6$	$2C_3$	C_2	$3\sigma_v$	$3\sigma_d$
A_1	+1	+1	+1	+1	+1	+1
A_2	+1	+1	+1	+1	-1	-1
B_1	+1	-1	+1	-1	+1	-1
B_2	+1	-1	+1	-1	-1	+1
E_1	+2	+1	-1	-2	0	0
E_2	+2	-1	-1	+2	0	0

Illustrations of several of these wavefunctions can be found in Appendix A. Evidently they all exhibit sixfold symmetry; that is, they correspond to certain representations of the C_{6v} point group, the character table of which is given by Table 3.1 [19]. In the table, E is the identity operation, $2C_6$ are the clockwise and counterclockwise rotations about the origin by 60°, $2C_3$ are rotations by 120°, C_2 is rotation by 180°, $3\sigma_v$ are reflections over the three lines connecting the midpoints of opposite edges, and $3\sigma_d$ are reflections over the three lines connecting opposite vertices. It can

be seen from the wavefunction plots (or shown analytically by a coordinate transformation) that the even modes correspond to the A_1 representation and the odd modes to the B_2 representation. Immediately we can see that these modes must not constitute a complete set of solutions, because none of these corresponds to the other one- and two-dimensional representations. Observe that both the even and odd modes have even symmetry about the lines connecting opposite vertices, yet it is not difficult to envision solutions with odd symmetry about these lines. Similarly, one would expect solutions corresponding to the two-dimensional representations (E_1 and E_2) as well, which do not have sixfold symmetry alone but can be made into linear combinations which do.

The reason that only the A_1 and B_2 representations can be expressed in closed form is related to the problem of tiling the plane. Both the even and odd closed-form solutions can tile the plane without any discontinuities, because the value of the wavefunction matches at all points on the boundary between two adjacent hexagons as a result of the even symmetry under σ_d, and the normal derivative is continuous as well by the boundary conditions. On the other hand, a wavefunction corresponding to the A_2 or B_1 representations would have odd symmetry under σ_d, and the values of the functions would be opposite in sign at the boundary.

In addition, the hexagonal domain can be divided into six equilateral triangles. For the A_1- and B_2-type hexagon wavefunctions, the Neumann boundary conditions are satisfied on all sides of each of the equilateral triangles (this follows from the even symmetry under σ_d—the normal derivative on the lines connecting opposite vertices, i.e. the boundaries of the subtriangles, must vanish). Since the wave equation is solvable in closed form for an equilateral triangle with Neumann boundary conditions on all three sides, the hexagon wavefunction can in principle be derived from these triangle wavefunctions. However, for the A_2- and B_1-type wavefunctions, the wavefunction itself rather than its derivative would have to be zero at the boundary of the subtriangles. This implies a mixed boundary condition where one side requires the Neumann boundary condition and the other two sides require the Dirichlet boundary condition. This is much more difficult to solve for the

equilateral triangle.

Radiation due to the uniform AC Josephson current

Because the alternating superconducting-insulating layers of the MSA behave as a stack of IJJs, when a voltage is applied across the MSA, an AC current appears normal to the layers in accordance with the Josephson effect. This uniform AC current is the primary source of radiation from the MSA. Because the thermally-managed MSAs are plated with gold on the top and the bottom in order to transfer heat away from the BSCCO, it can be assumed that the radiation is emitted entirely from the edges of the MSA. To obtain the power distribution due to the primary radiation source, we begin by computing the magnetic vector potential

$$A_z(\boldsymbol{r}, t) = \frac{\mu_0}{4\pi} \frac{e^{i(k_{mn}r - \omega_{mn}t)}}{r} \int_S dx\, dy\, e^{-i\boldsymbol{k}_{mn}\cdot\boldsymbol{r}} J_J \tag{3.9}$$

which has only a z-component, where J_J is the uniform Josephson current, k_{mn} and ω_{mn} are the wavevector and frequency respectively of the (m, n)-mode, and the integration is over the surface of the hexagon. From this point onward we shall suppress the subscripts on k and ω for clarity, but their values depend on the mode in question. With the assumption that only the boundary of the hexagonal region contributes anything to the integral, the surface integral reduces essentially to a line integral around the perimeter. We break the integration path into six paths, each corresponding

to an edge of the hexagon:

$$
\begin{aligned}
\overline{AB} : &\quad \hat{\boldsymbol{y}}\,\delta\!\left(x - \frac{a\sqrt{3}}{2}\right) \\[6pt]
\overline{BC} : &\quad \left(-\frac{\sqrt{3}}{2}\hat{\boldsymbol{x}} + \frac{1}{2}\hat{\boldsymbol{y}}\right)\delta\!\left(y + \frac{1}{\sqrt{3}}x - a\right) \\[6pt]
\overline{CD} : &\quad \left(-\frac{\sqrt{3}}{2}\hat{\boldsymbol{x}} - \frac{1}{2}\hat{\boldsymbol{y}}\right)\delta\!\left(y - \frac{1}{\sqrt{3}}x - a\right) \\[6pt]
\overline{DE} : &\quad -\hat{\boldsymbol{y}}\,\delta\!\left(x + \frac{a\sqrt{3}}{2}\right) \\[6pt]
\overline{EF} : &\quad \left(\frac{\sqrt{3}}{2}\hat{\boldsymbol{x}} - \frac{1}{2}\hat{\boldsymbol{y}}\right)\delta\!\left(y + \frac{1}{\sqrt{3}}x + a\right) \\[6pt]
\overline{FA} : &\quad \left(\frac{\sqrt{3}}{2}\hat{\boldsymbol{x}} + \frac{1}{2}\hat{\boldsymbol{y}}\right)\delta\!\left(y - \frac{1}{\sqrt{3}}x + a\right)
\end{aligned}
\tag{3.10}
$$

The integrals are much simpler for paths $\overline{AB}$ and $\overline{DE}$ because the paths are parallel to one of the coordinate axes (and thus the value of the other coordinate is constant). This motivates us to define a new set of coordinates

$$
x_{\pm} = \frac{\sqrt{3}}{2}x \pm \frac{1}{2}y \tag{3.11}
$$

$$
y_{\pm} = \mp\frac{1}{2}x + \frac{\sqrt{3}}{2}y \tag{3.12}
$$

where x_+ and y_+ correspond to a rotation of the hexagon about the origin by $30°$ clockwise and x_- and y_- to a rotation by $30°$ counterclockwise.

The inverses of these transformations are
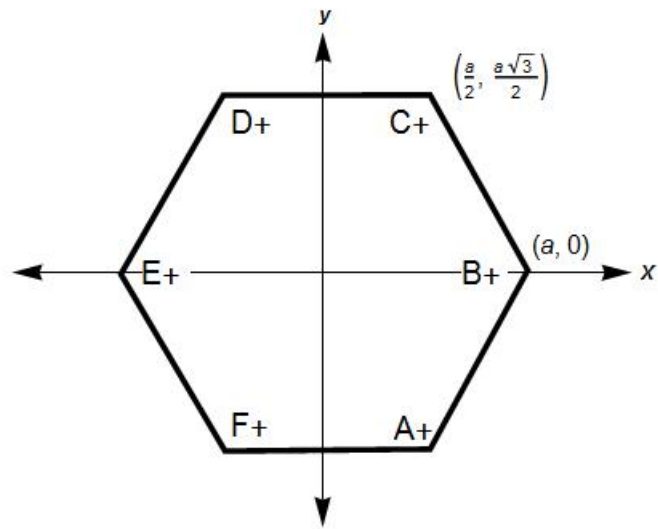
Figure 3.2: Hexagon rotated 30° clockwise.
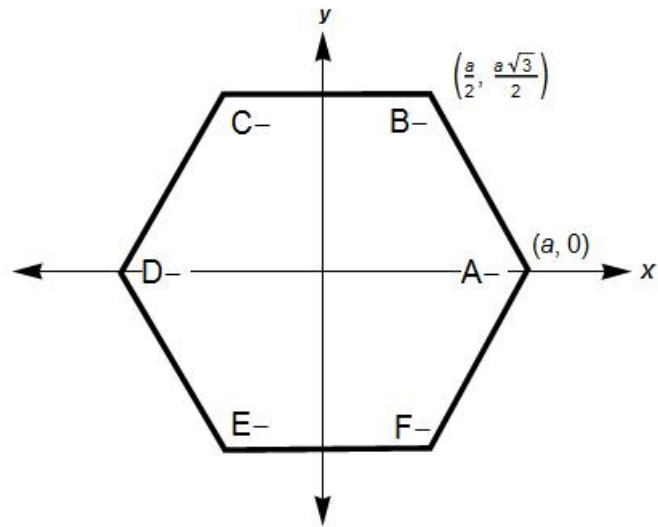
Figure 3.3: Hexagon rotated 30° counterclockwise.

13

$$x = \frac{\sqrt{3}}{2} x_\pm \mp \frac{1}{2} y_\pm \tag{3.13}$$

$$y = \pm \frac{1}{2} x_\pm + \frac{\sqrt{3}}{2} y_\pm, \tag{3.14}$$

and with these new coordinates the six paths can be reformulated as

$$
\begin{aligned}
\overline{AB} : && \hat{\boldsymbol{y}}\, \delta\left(x - \frac{a\sqrt{3}}{2}\right) \\
\overline{B_-C_-} : && -\hat{\boldsymbol{x}}_-\, \delta\left(y_- - \frac{a\sqrt{3}}{2}\right) \\
\overline{C_+D_+} : && -\hat{\boldsymbol{x}}_+\, \delta\left(y_+ - \frac{a\sqrt{3}}{2}\right) \\
\overline{DE} : && -\hat{\boldsymbol{y}}\, \delta\left(x + \frac{a\sqrt{3}}{2}\right) \\
\overline{E_-F_-} : && \hat{\boldsymbol{x}}_-\, \delta\left(y_- + \frac{a\sqrt{3}}{2}\right) \\
\overline{F_+A_+} : && \hat{\boldsymbol{x}}_+\, \delta\left(y_+ + \frac{a\sqrt{3}}{2}\right)
\end{aligned}
\tag{3.15}
$$

In computing the necessary integrals it will be helpful to define the new variables

$$
\begin{aligned}
X_\pm &= \frac{\pi\sqrt{m^2 + n^2 + mn}}{3 n_r} \sin\theta \left(\pm \frac{\cos\varphi}{\sqrt{3}} + \sin\varphi\right) \\
&= \frac{ka}{4} \sin\theta \left(\pm \frac{\cos\varphi}{\sqrt{3}} + \sin\varphi\right)
\end{aligned}
\tag{3.16}
$$

14

$$Y_\pm = \frac{\pi\sqrt{m^2 + n^2 + mn}}{3n_r} \sin\theta \left(\sqrt{3}\cos\varphi \pm \sin\varphi\right)$$
$$= \frac{ka}{4} \sin\theta \left(\sqrt{3}\cos\varphi \pm \sin\varphi\right) \tag{3.17}$$

We first integrate along the path $\overline{AB}$, using the unmodified coordinates. Expressing the components of the wavevector as $k_x = k\sin\theta\cos\varphi$ and $k_y = k\sin\theta\sin\varphi$, we obtain

$$\iint_A^B dx\, dy\, \delta\left(x - \frac{a\sqrt{3}}{2}\right) e^{-i(k_x x + k_y y)}$$
$$= \int dx\, \delta\left(x - \frac{a\sqrt{3}}{2}\right) e^{-ik\sin\theta\cos\varphi\, x} \int_{-a/2}^{a/2} dy\, e^{-ik\sin\theta\sin\varphi\, y}$$
$$= e^{-ika\sqrt{3}\sin\theta\cos\varphi/2} \int_{-a/2}^{a/2} dy\, e^{-i\frac{2}{a}(Y_+ - Y_-)y} \tag{3.18}$$
$$= e^{-3i(X_+ - X_-)} \frac{-a}{2i(Y_+ - Y_-)} \left[e^{-i(Y_+ - Y_-)} - e^{i(Y_+ - Y_-)}\right]$$
$$= a e^{-3i(X_+ - X_-)} \frac{\sin(Y_+ - Y_-)}{(Y_+ - Y_-)}$$

The integral along $\overline{DE}$ can be evaluated similarly; it equals the complex conjugate of that along $\overline{AB}$, so the sum of their contributions is a single term involving a cosine rather than exponentials (this occurs for all three pairs of opposite sides). The integral along $\overline{BC}$ can be evaluated using the

15

transformed coordinates, remembering to transform $k_{-,x}$ and $k_{-,y}$ according to equation 3.11:

$$
\iint_{B_-}^{C_-} (-dx_-)\, dy_-\, \delta\left(y_- - \frac{a\sqrt{3}}{2}\right) e^{-i[(\frac{\sqrt{3}}{2}k_x - \frac{1}{2}k_y)x_- + (\frac{1}{2}k_x + \frac{\sqrt{3}}{2}k_y)y_-]}
$$

$$
= \int dy_-\, \delta\left(y_- - \frac{a\sqrt{3}}{2}\right) e^{-ik\sin\theta(\cos\varphi + \sqrt{3}\sin\varphi)y_-/2} \int_{a/2}^{-a/2} (-dx_-)\, e^{-ik\sin\theta(\sqrt{3}\cos\varphi - \sin\varphi)x_-/2}
$$

$$
= e^{-ika\sin\theta(\sqrt{3}\cos\varphi + 3\sin\varphi)/4} \int_{-a/2}^{a/2} dx_-\, e^{-i\frac{2}{a}Y_- x_-} = e^{-3iX_+} \frac{-a}{2iY_-}\left[e^{-iY_-} - e^{iY_-}\right]
$$

$$
= ae^{-3iX_+} \frac{\sin(Y_-)}{Y_-}
$$

$$(3.19)$$

The rest of the integrals can be computed similarly, and we find that

$$
\boldsymbol{A}(\boldsymbol{r}, t) \propto (\hat{\boldsymbol{\theta}}\sin\theta) \frac{e^{i(kr - \omega t)}}{r}\left[\cos[3(X_+ - X_-)]\frac{\sin(Y_+ - Y_-)}{Y_+ - Y_-}\right.
$$
$$
\left. + \cos(3X_+)\frac{\sin(Y_-)}{Y_-} + \cos(3X_-)\frac{\sin(Y_+)}{Y_+}\right] \quad (3.20)
$$

where we have used $\hat{\boldsymbol{z}} = -\hat{\boldsymbol{\theta}}\sin\theta$ and absorbed constants into the proportionality sign. The electric field and the magnetic field (assuming the latter to have only a φ-component) are

$$
\boldsymbol{E} = -\frac{\partial \boldsymbol{A}}{\partial t} = i\omega\boldsymbol{A} \tag{3.21}
$$

$$
\boldsymbol{H} = \frac{1}{\mu_0}\nabla \times \boldsymbol{A} \propto \frac{1}{r}\left[\frac{\partial}{\partial r}(rA_\theta) - \frac{\partial A_r}{\partial \theta}\right]\hat{\boldsymbol{\varphi}} = ik|\boldsymbol{A}|\hat{\boldsymbol{\varphi}} \tag{3.22}
$$

16

and finally we can obtain the power distribution for the radiation from the uniform AC Josephson current source:

$$P(\theta, \varphi) = |r^2 \hat{\boldsymbol{r}} \cdot \boldsymbol{E} \times \boldsymbol{H}^*|$$

$$\propto \sin^2 \theta \left| \cos[3(X_+ - X_-)] \frac{\sin(Y_+ - Y_-)}{Y_+ - Y_-} + \cos(3X_+) \frac{\sin(Y_-)}{Y_-} + \cos(3X_-) \frac{\sin(Y_+)}{Y_+} \right|^2 \quad (3.23)$$

Several plots of these distributions can be found in Appendix B. The sixfold symmetry is readily apparent.

Radiation due to electromagnetic cavity mode excitation

The secondary source of radiation is due to the excitation of one of the modes of the electromagnetic cavity. If the characteristic frequency of one of the cavity modes equals an integer multiple of the AC Josephson frequency, radiation is emitted. Applying Love's equivalence principle for electric conductors, the electric field can be replaced by a magnetic surface current density. For a given cavity mode, current density is the path around the edge of the mesa (equations 3.10 or 3.15) weighted by the wavefunction (equations 3.5 and 3.6), that is,

$$\boldsymbol{M}(\boldsymbol{r}, t) = \Psi_{mn}^{e,o}(x, y) \times \left(\overline{AB} + \overline{BC} + \cdots + \overline{FA} \right), \quad (3.24)$$

and from this the electric vector potential can be obtained by

$$\boldsymbol{F}(\boldsymbol{r},t) = \frac{\epsilon_0}{4\pi} \frac{e^{i(kr-\omega t)}}{r} \int_S dx\, dy\, \boldsymbol{M}(x,y) e^{-i\boldsymbol{k}\cdot\boldsymbol{r}}. \tag{3.25}$$

Again the integral over the surface reduces to a line integral along the boundary, which is seg-mented into six paths. Once the electric vector potential is calculated, the electric and magnetic fields, and thus the power, follow. For brevity, we shall not show the computation of the integrals, but the results can be found in Appendix A, and several plots, which reflect the sixfold symmetry, can be found in Appendix B.

CHAPTER 4: DISCUSSION

We began by presenting the closed-form solutions of the wave equation on a regular hexagonal domain and derived formulas for the radiated power arising from two different mechanisms: the uniform part of the AC Josephson current and the excited electromagnetic cavity modes. As expected, the resulting angular distributions of radiation possess the C_{6v} point group symmetry of the hexagonal MSA. However, these closed-form wavefunctions correspond only to the one-dimensional A_1 and B_2 representations of the group, and the remaining solutions must be expressed as infinite series. Unfortunately these non-closed-form solutions cannot be neglected, since they are still valid solutions to the wave equation and the Neumann boundary conditions, and there is no reason to assume that they are not interspersed among the closed-form solutions in terms of energy. Therefore the next logical step in the theory of the hexagonal MSA is to find expressions for these more troublesome solutions and to compute the radiated power from them. One potential strategy for doing so is to divide the hexagon into its six constituent equilateral subtriangles and solve the wave equation on this equilateral triangular domain with a mixed boundary condition—Neumann on one side, Dirichlet on the other two. By reassembling these solutions, more hexagon solutions can be obtained corresponding to other representations of C_{6v}.

Conveniently, there is one physical reason that the closed-form solutions are of particular interest. If another boundary condition is imposed, namely that the normal derivative vanish on the three lines connecting opposite vertices of the hexagon, then these closed-form solutions are the *only* solutions. Hexagonal arrays of MSAs composed of six equilateral triangular patches have been studied experimentally [20], and if we suppose that the gap between adjacent triangles is significant, then the Neumann boundary condition ought to be satisfied at these gaps.

APPENDIX A: CAVITY MODE SOURCE POWER CALCULATION

APPENDIX A: CAVITY MODE SOURCE POWER CALCULATION

For both the even and the odd modes, the electric potential is

$$\boldsymbol{F}^{e,o}(\boldsymbol{r},t) \propto \frac{e^{i(kr-\omega t)}}{r} \left[\hat{\boldsymbol{y}} A^{e,o} - \left(\sqrt{3}\hat{\boldsymbol{x}} - \hat{\boldsymbol{y}} \right) B^{e,o} - \left(\sqrt{3}\hat{\boldsymbol{x}} + \hat{\boldsymbol{y}} \right) C^{e,o} \right.$$
$$\left. - \hat{\boldsymbol{y}} D^{e,o} + \left(\sqrt{3}\hat{\boldsymbol{x}} - \hat{\boldsymbol{y}} \right) E^{e,o} + \left(\sqrt{3}\hat{\boldsymbol{x}} + \hat{\boldsymbol{y}} \right) F^{e,o} \right] \quad \text{(A.1)}$$

where we have defined six functions for each of the even and odd modes—$A^e(\theta, \varphi)$ through $F^e(\theta, \varphi)$ and $A^o(\theta, \varphi)$ through $F^o(\theta, \varphi)$—which result from the integration:

$$A^e = 4e^{-3i(X_+ - X_-)} \sum_{\sigma=\pm} \left[(-1)^{m+n} \frac{\sin(Y_{+,\sigma(m-n)} - Y_{-,-\sigma(m-n)})}{Y_{+,\sigma(m-n)} - Y_{-,-\sigma(m-n)}} \right.$$
$$\left. + (-1)^m \frac{\sin(Y_{+,\sigma(m+2n)} - Y_{-,-\sigma(m+2n)})}{Y_{+,\sigma(m+2n)} - Y_{-,-\sigma(m+2n)}} + (-1)^n \frac{\sin(Y_{+,\sigma(2m+n)} - Y_{-,-\sigma(2m+n)})}{Y_{+,\sigma(2m+n)} - Y_{-,-\sigma(2m+n)}} \right] \quad \text{(A.2)}$$

$$B^e = e^{-3iX_+} \sum_{\sigma,\sigma'=\pm} \left[e^{i\pi[(m+n)\sigma+(m-n)\sigma']/2} \frac{\sin(Y_{-,3(m+n)\sigma-(m-n)\sigma'})}{Y_{-,3(m+n)\sigma-(m-n)\sigma'}} \right.$$
$$\left. + e^{i\pi[m\sigma+(m+2n)\sigma']/2} \frac{\sin(Y_{-,3m\sigma-(m+2n)\sigma'})}{Y_{-,3m\sigma-(m+2n)\sigma'}} + e^{i\pi[n\sigma+(2m+n)\sigma']/2} \frac{\sin(Y_{-,3n\sigma-(2m+n)\sigma'})}{Y_{-,3n\sigma-(2m+n)\sigma'}} \right] \quad \text{(A.3)}$$

$$C^e = e^{-3iX_-} \sum_{\sigma,\sigma'=\pm} \left[e^{i\pi[-(m+n)\sigma+(m-n)\sigma']/2} \frac{\sin(Y_{+,3(m+n)\sigma+(m-n)\sigma'})}{Y_{+,3(m+n)\sigma+(m-n)\sigma'}} \right.$$

$$\left. + e^{i\pi[-m\sigma+(m+2n)\sigma']/2} \frac{\sin(Y_{+,3m\sigma+(m+2n)\sigma'})}{Y_{+,3m\sigma+(m+2n)\sigma'}} + e^{i\pi[-n\sigma+(2m+n)\sigma']/2} \frac{\sin(Y_{+,3n\sigma+(2m+n)\sigma'})}{Y_{+,3n\sigma+(2m+n)\sigma'}} \right] \quad (A.4)$$

$$D^e = 4e^{3i(X_+ - X_-)} \sum_{\sigma=\pm} \left[(-1)^{m+n} \frac{\sin(Y_{+,\sigma(m-n)} - Y_{-,-\sigma(m-n)})}{Y_{+,\sigma(m-n)} - Y_{-,-\sigma(m-n)}} \right.$$

$$\left. + (-1)^m \frac{\sin(Y_{+,\sigma(m+2n)} - Y_{-,-\sigma(m+2n)})}{Y_{+,\sigma(m+2n)} - Y_{-,-\sigma(m+2n)}} + (-1)^n \frac{\sin(Y_{+,\sigma(2m+n)} - Y_{-,-\sigma(2m+n)})}{Y_{+,\sigma(2m+n)} - Y_{-,-\sigma(2m+n)}} \right] \quad (A.5)$$

$$E^e = e^{3iX_+} \sum_{\sigma,\sigma'=\pm} \left[e^{i\pi[-(m+n)\sigma+(m-n)\sigma']/2} \frac{\sin(Y_{-,3(m+n)\sigma+(m-n)\sigma'})}{Y_{-,3(m+n)\sigma+(m-n)\sigma'}} \right.$$

$$\left. + e^{i\pi[-m\sigma+(m+2n)\sigma']/2} \frac{\sin(Y_{-,3m\sigma+(m+2n)\sigma'})}{Y_{-,3m\sigma+(m+2n)\sigma'}} + e^{i\pi[-n\sigma+(2m+n)\sigma']/2} \frac{\sin(Y_{-,3n\sigma+(2m+n)\sigma'})}{Y_{-,3n\sigma+(2m+n)\sigma'}} \right] \quad (A.6)$$

$$F^e = e^{3iX_-} \sum_{\sigma,\sigma'=\pm} \left[e^{i\pi[(m+n)\sigma-(m-n)\sigma']/2} \frac{\sin(Y_{+,3(m+n)\sigma+(m-n)\sigma'})}{Y_{+,3(m+n)\sigma+(m-n)\sigma'}} \right.$$

$$\left. + e^{i\pi[m\sigma-(m+2n)\sigma']/2} \frac{\sin(Y_{+,3m\sigma+(m+2n)\sigma'})}{Y_{+,3m\sigma+(m+2n)\sigma'}} + e^{i\pi[n\sigma-(2m+n)\sigma']/2} \frac{\sin(Y_{+,3n\sigma+(2m+n)\sigma'})}{Y_{+,3n\sigma+(2m+n)\sigma'}} \right] \quad (A.7)$$

$$A^o = \frac{4}{i} e^{-3i(X_+ - X_-)} \sum_{\sigma=\pm} \sigma \left[(-1)^{m+n} \frac{\sin(Y_{+,\sigma(m-n)} - Y_{-,-\sigma(m-n)})}{Y_{+,\sigma(m-n)} - Y_{-,-\sigma(m-n)}} \right.$$
$$\left. + (-1)^m \frac{\sin(Y_{+,\sigma(m+2n)} - Y_{-,-\sigma(m+2n)})}{Y_{+,\sigma(m+2n)} - Y_{-,-\sigma(m+2n)}} - (-1)^n \frac{\sin(Y_{+,\sigma(2m+n)} - Y_{-,-\sigma(2m+n)})}{Y_{+,\sigma(2m+n)} - Y_{-,-\sigma(2m+n)}} \right] \quad \text{(A.8)}$$

$$B^o = -\frac{1}{i} e^{-3iX_+} \sum_{\sigma,\sigma'=\pm} \sigma' \left[e^{i\pi[(m+n)\sigma+(m-n)\sigma']/2} \frac{\sin(Y_{-,3(m+n)\sigma-(m-n)\sigma'})}{Y_{-,3(m+n)\sigma-(m-n)\sigma'}} \right.$$
$$\left. + e^{i\pi[m\sigma+(m+2n)\sigma']/2} \frac{\sin(Y_{-,3m\sigma-(m+2n)\sigma'})}{Y_{-,3m\sigma-(m+2n)\sigma'}} - e^{i\pi[n\sigma+(2m+n)\sigma']/2} \frac{\sin(Y_{-,3n\sigma-(2m+n)\sigma'})}{Y_{-,3n\sigma-(2m+n)\sigma'}} \right] \quad \text{(A.9)}$$

$$C^o = \frac{1}{i} e^{-3iX_-} \sum_{\sigma,\sigma'=\pm} \sigma' \left[e^{i\pi[-(m+n)\sigma+(m-n)\sigma']/2} \frac{\sin(Y_{+,3(m+n)\sigma+(m-n)\sigma'})}{Y_{+,3(m+n)\sigma+(m-n)\sigma'}} \right.$$
$$\left. + e^{i\pi[-m\sigma+(m+2n)\sigma']/2} \frac{\sin(Y_{+,3m\sigma+(m+2n)\sigma'})}{Y_{+,3m\sigma+(m+2n)\sigma'}} - e^{i\pi[-n\sigma+(2m+n)\sigma']/2} \frac{\sin(Y_{+,3n\sigma+(2m+n)\sigma'})}{Y_{+,3n\sigma+(2m+n)\sigma'}} \right] \quad \text{(A.10)}$$

$$D^o = -\frac{4}{i} e^{3i(X_+ - X_-)} \sum_{\sigma=\pm} \sigma \left[(-1)^{m+n} \frac{\sin(Y_{+,\sigma(m-n)} - Y_{-,-\sigma(m-n)})}{Y_{+,\sigma(m-n)} - Y_{-,-\sigma(m-n)}} \right.$$
$$\left. + (-1)^m \frac{\sin(Y_{+,\sigma(m+2n)} - Y_{-,-\sigma(m+2n)})}{Y_{+,\sigma(m+2n)} - Y_{-,-\sigma(m+2n)}} - (-1)^n \frac{\sin(Y_{+,\sigma(2m+n)} - Y_{-,-\sigma(2m+n)})}{Y_{+,\sigma(2m+n)} - Y_{-,-\sigma(2m+n)}} \right] \quad \text{(A.11)}$$

$$E^o = -\frac{1}{i}e^{3iX_+} \sum_{\sigma,\sigma'=\pm} \sigma' \left[e^{i\pi[-(m+n)\sigma+(m-n)\sigma']/2} \frac{\sin(Y_{-,3(m+n)\sigma+(m-n)\sigma'})}{Y_{-,3(m+n)\sigma+(m-n)\sigma'}} \right.$$

$$\left. + e^{i\pi[-m\sigma+(m+2n)\sigma']/2} \frac{\sin(Y_{-,3m\sigma+(m+2n)\sigma'})}{Y_{-,3m\sigma+(m+2n)\sigma'}} - e^{i\pi[-n\sigma+(2m+n)\sigma']/2} \frac{\sin(Y_{-,3n\sigma+(2m+n)\sigma'})}{Y_{-,3n\sigma+(2m+n)\sigma'}} \right] \quad \text{(A.12)}$$

$$F^o = -\frac{1}{i}e^{3iX_-} \sum_{\sigma,\sigma'=\pm} \sigma' \left[e^{i\pi[(m+n)\sigma-(m-n)\sigma']/2} \frac{\sin(Y_{+,3(m+n)\sigma+(m-n)\sigma'})}{Y_{+,3(m+n)\sigma+(m-n)\sigma'}} \right.$$

$$\left. + e^{i\pi[m\sigma-(m+2n)\sigma']/2} \frac{\sin(Y_{+,3m\sigma+(m+2n)\sigma'})}{Y_{+,3m\sigma+(m+2n)\sigma'}} - e^{i\pi[n\sigma-(2m+n)\sigma']/2} \frac{\sin(Y_{+,3n\sigma+(2m+n)\sigma'})}{Y_{+,3n\sigma+(2m+n)\sigma'}} \right] \quad \text{(A.13)}$$

We express $\hat{\boldsymbol{x}}$ and $\hat{\boldsymbol{y}}$ in spherical coordinates, neglecting the r-components of both these unit vectors because of the approximation $r \gg a$. When computing the curl in spherical coordinates, four of the six terms go like $1/r$, including both of the terms involving derivatives of F_r. In other words, with the far-field approximation, $\nabla \times \boldsymbol{F} \approx -\frac{1}{r}\frac{\partial}{\partial r}(rF_\varphi)\hat{\boldsymbol{\theta}} + \frac{1}{r}\frac{\partial}{\partial r}(rF_\theta)\hat{\boldsymbol{\varphi}}$. Hence we obtain

$$\boldsymbol{F}^{e,o}(\boldsymbol{r},t) \propto \frac{e^{i(kr-\omega t)}}{r} \left\{ (\cos\theta\sin\varphi\,\hat{\boldsymbol{\theta}} + \cos\varphi\,\hat{\boldsymbol{\varphi}})A^{e,o} \right.$$

$$- \left[\sqrt{3}(\cos\theta\cos\varphi\,\hat{\boldsymbol{\theta}} - \sin\varphi\,\hat{\boldsymbol{\varphi}}) - (\cos\theta\sin\varphi\,\hat{\boldsymbol{\theta}} + \cos\varphi\,\hat{\boldsymbol{\varphi}}) \right] B^{e,o}$$

$$- \left[\sqrt{3}(\cos\theta\cos\varphi\,\hat{\boldsymbol{\theta}} - \sin\varphi\,\hat{\boldsymbol{\varphi}}) + (\cos\theta\sin\varphi\,\hat{\boldsymbol{\theta}} + \cos\varphi\,\hat{\boldsymbol{\varphi}}) \right] C^{e,o}$$

$$- (\cos\theta\sin\varphi\,\hat{\boldsymbol{\theta}} + \cos\varphi\,\hat{\boldsymbol{\varphi}})D^{e,o}$$

$$+ \left[\sqrt{3}(\cos\theta\cos\varphi\,\hat{\boldsymbol{\theta}} - \sin\varphi\,\hat{\boldsymbol{\varphi}}) - (\cos\theta\sin\varphi\,\hat{\boldsymbol{\theta}} + \cos\varphi\,\hat{\boldsymbol{\varphi}}) \right] E^{e,o}$$

$$\left. + \left[\sqrt{3}(\cos\theta\cos\varphi\,\hat{\boldsymbol{\theta}} - \sin\varphi\,\hat{\boldsymbol{\varphi}}) + (\cos\theta\sin\varphi\,\hat{\boldsymbol{\theta}} + \cos\varphi\,\hat{\boldsymbol{\varphi}}) \right] F^{e,o} \right\} \quad \text{(A.14)}$$

If we gather together the θ- and φ-components and define two new expressions

$$\Theta^{e,o}(\theta, \varphi) = \cos\theta \sin\varphi \, A^{e,o} - \sqrt{3}\cos\theta \cos\varphi \, B^{e,o} + \cos\theta \sin\varphi \, B^{e,o}$$
$$- \sqrt{3}\cos\theta \cos\varphi \, C^{e,o} - \cos\theta \sin\varphi \, C^{e,o} - \cos\theta \sin\varphi \, D^{e,o}$$
$$+ \sqrt{3}\cos\theta \cos\varphi \, E^{e,o} - \cos\theta \sin\varphi \, E^{e,o} + \sqrt{3}\cos\theta \cos\varphi \, F^{e,o} + \cos\theta \sin\varphi \, F^{e,o} \quad (A.15)$$

$$\Phi^{e,o}(\varphi) = \cos\varphi \, A^{e,o} + \sqrt{3}\sin\varphi \, B^{e,o} + \cos\varphi \, B^{e,o} + \sqrt{3}\sin\varphi \, C^{e,o} - \cos\varphi \, C^{e,o}$$
$$- \cos\varphi \, D^{e,o} - \sqrt{3}\sin\varphi \, E^{e,o} - \cos\varphi \, E^{e,o} - \sqrt{3}\sin\varphi \, F^{e,o} + \cos\varphi \, F^{e,o} \quad (A.16)$$

then we can write this concisely as

$$\boldsymbol{F}^{e,o}(\boldsymbol{r}, t) \propto \frac{e^{i(kr-\omega t)}}{r} \left[\Theta^{e,o}(\theta, \varphi)\hat{\boldsymbol{\theta}} + \Phi^{e,o}(\varphi)\hat{\boldsymbol{\varphi}}\right] \quad (A.17)$$

The electric field can be obtained from $\boldsymbol{E} = -\frac{1}{\epsilon_0}\nabla \times \boldsymbol{F}$; the magnetic field can be obtained from Faraday's Law, i.e. $-\frac{\partial \boldsymbol{H}}{\partial t} = \nabla \times \boldsymbol{E}$:

$$\boldsymbol{E}(\boldsymbol{r}, t) \propto i\frac{e^{i(kr-\omega t)}}{r} \left[\Phi^{e,o}(\varphi)\,\hat{\boldsymbol{\theta}} - \Theta^{e,o}(\theta, \varphi)\,\hat{\boldsymbol{\varphi}}\right] \quad (A.18)$$

$$\boldsymbol{H}(\boldsymbol{r}, t) \propto i\frac{e^{i(kr-\omega t)}}{r} \left[\Theta^{e,o}(\theta, \varphi)\,\hat{\boldsymbol{\theta}} + \Phi^{e,o}(\varphi)\,\hat{\boldsymbol{\varphi}}\right] \quad (A.19)$$

25

Finally, the power is

$$P^{e,o}(\theta, \varphi) \propto |\Phi^{e,o}(\varphi)|^2 + |\Theta^{e,o}(\theta, \varphi)|^2 \tag{A.20}$$

APPENDIX B: PLOTS OF WAVEFUNCTIONS AND POWER DISTRIBUTIONS

APPENDIX B: PLOTS OF WAVEFUNCTIONS AND POWER DISTRIBUTIONS

Here we provide illustrations of the wavefunctions and the resulting power distributions due to both sources for the sixteen lowest-energy modes. In the case of modes with $m = n$, the odd wavefunction vanishes, so neither it nor the cavity mode power is plotted. The wavefunction plots are contour plots in which the red regions represent positive values, the blue regions represent negative values, and any contours separating red and blue regions are nodal curves. Note that we only plot modes with $m \geq n$, since it is clear from equations 3.5 and 3.6 that the TM(m, n) mode's wavefunction is the same as that of the TM(n, m) mode (or its negative, for odd modes) and the energy is the same. No accidental degeneracies occur among these first sixteen modes, but they do occur for some higher modes—the first few are the TM(7,0) and TM(5,3) modes ($k \propto \sqrt{49}/a$), the TM(9,1) and TM(6,5) modes ($k \propto \sqrt{91}/a$), and the TM(11,1) and TM(9,4) modes ($k \propto \sqrt{133}/a$).
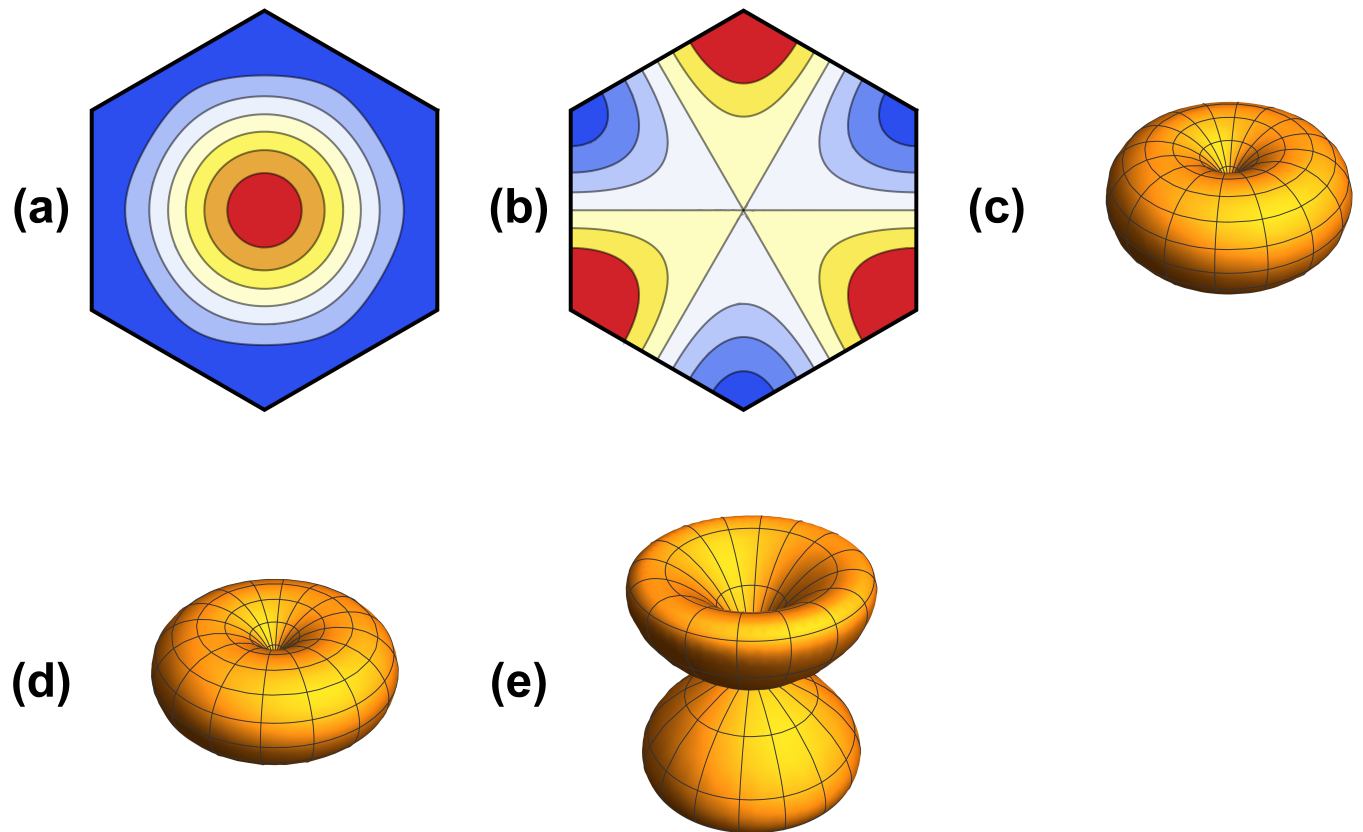
Figure B.1: Contour plots of the wavefunctions for the (a) even and (b) odd TM(1,0) modes ($k_{10} \propto \sqrt{1}/a$); (c) radiated power due to the uniform Josephson current for both the even and odd modes; and radiated power due to the cavity mode source for the (d) even and (e) odd modes.
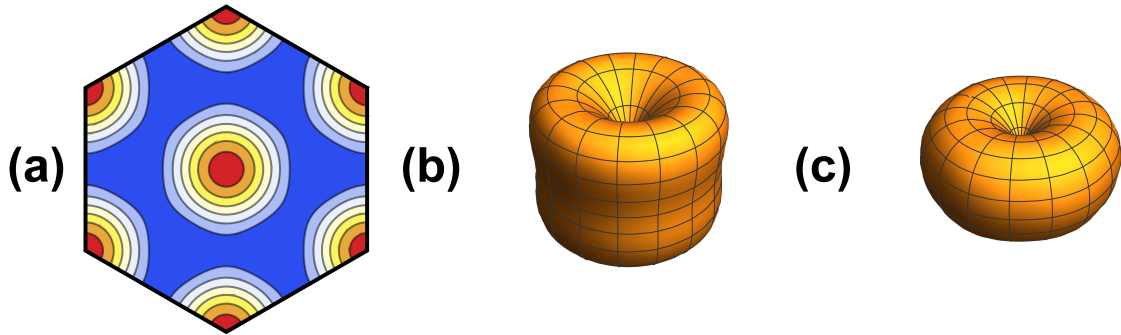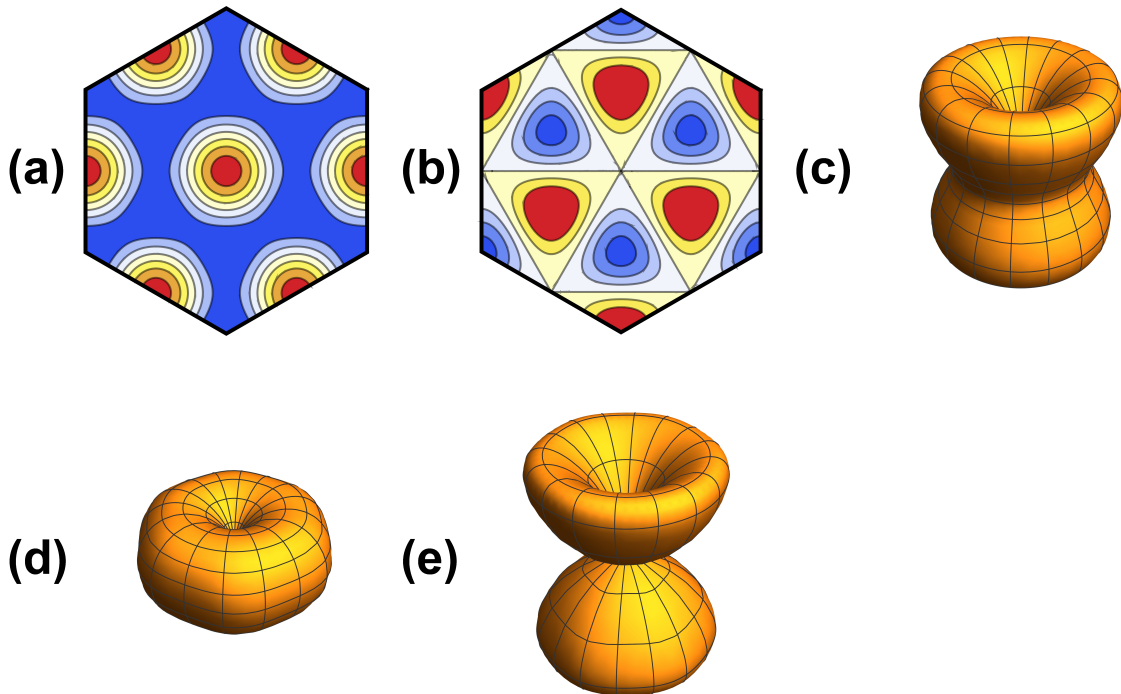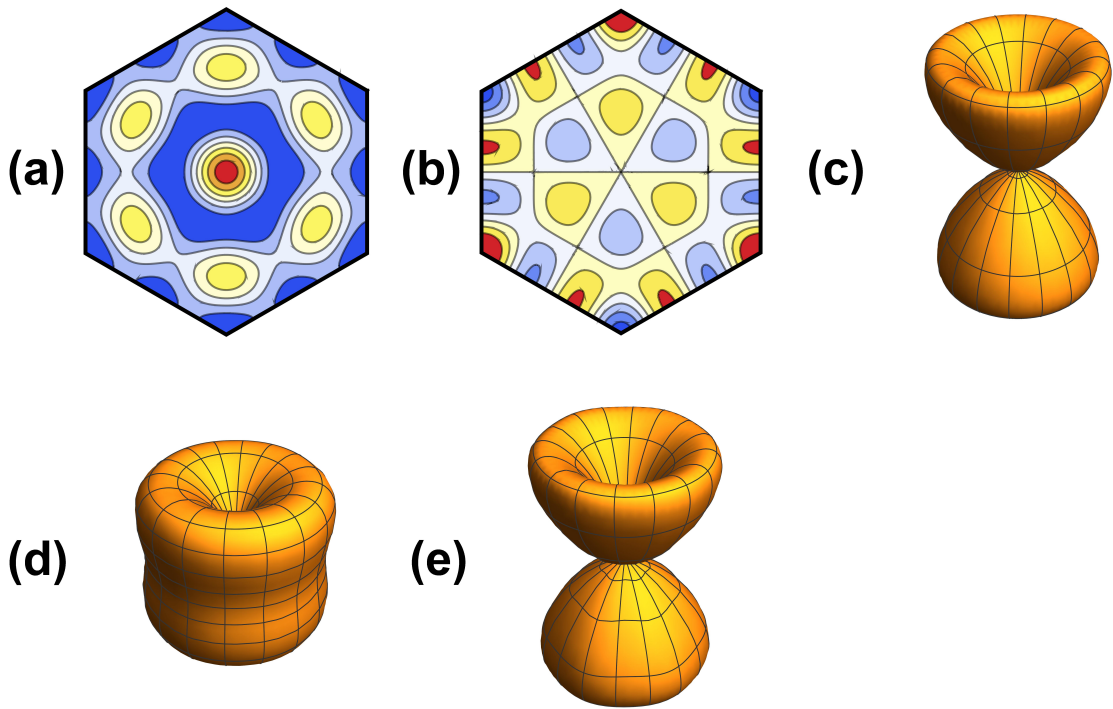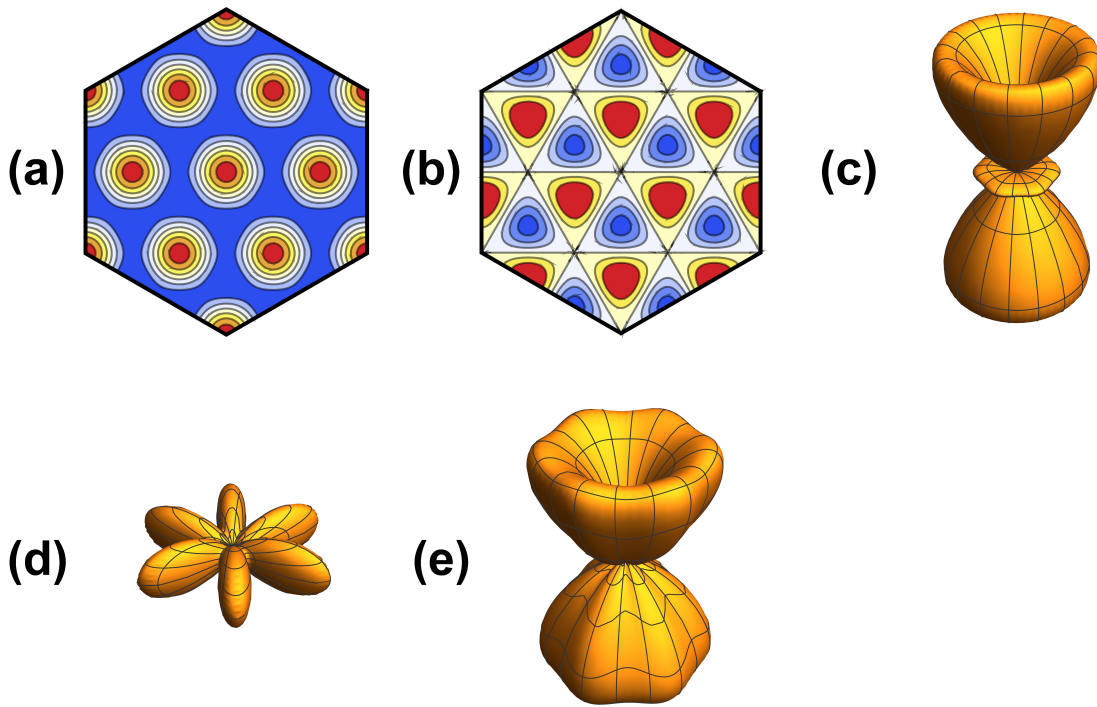
Figure B.2: (a) Contour plot of the wavefunction for the even TM(1,1) mode ($k_{11} \propto \sqrt{3}/a$); (b) radiated power due to the uniform Josephson current; and (c) radiated power due to the cavity mode source for the even mode.

Figure B.3: Contour plots of the wavefunctions for the (a) even and (b) odd TM(2,0) modes ($k_{20} \propto \sqrt{4}/a$); (c) radiated power due to the uniform Josephson current for both the even and odd modes; and radiated power due to the cavity mode source for the (d) even and (e) odd modes.
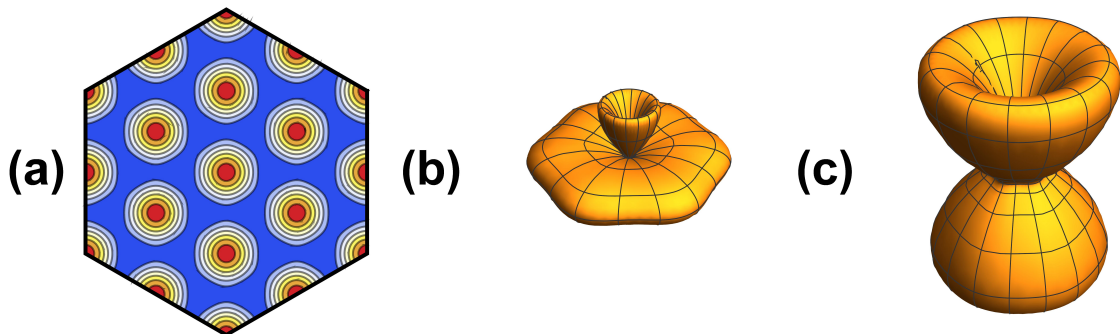
Figure B.4: Contour plots of the wavefunctions for the (a) even and (b) odd TM(2,1) modes ($k_{21} \propto \sqrt{7}/a$); (c) radiated power due to the uniform Josephson current for both the even and odd modes; and radiated power due to the cavity mode source for the (d) even and (e) odd modes.
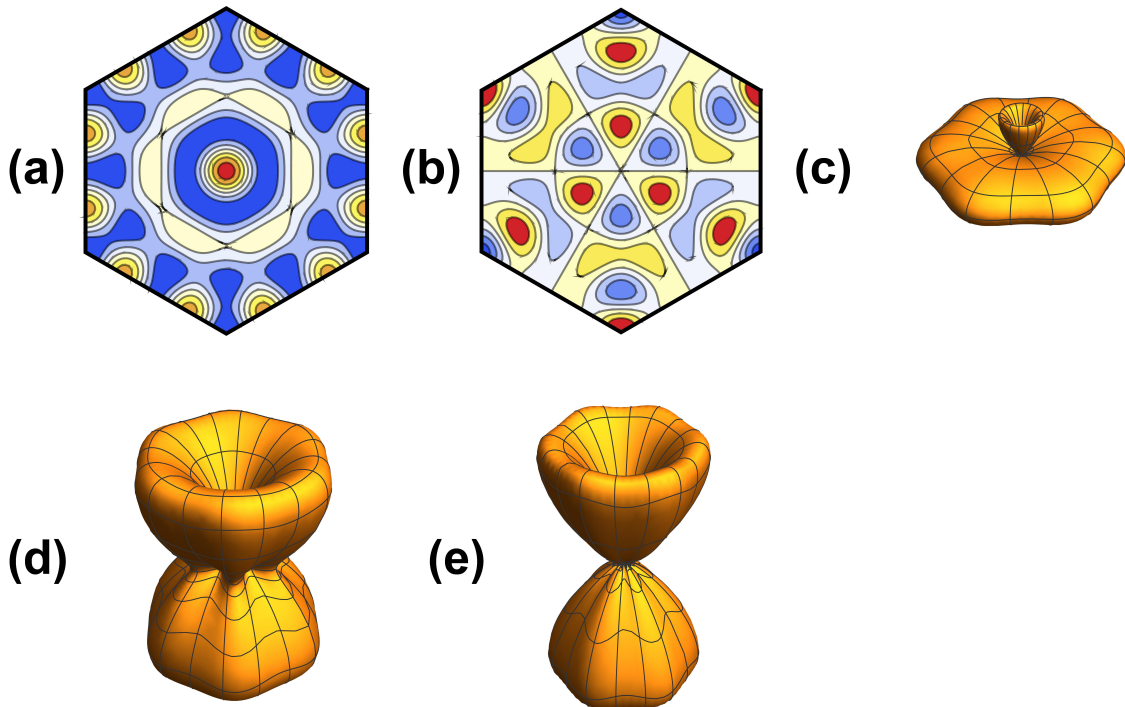
Figure B.5: Contour plots of the wavefunctions for the (a) even and (b) odd TM(3,0) modes ($k_{30} \propto \sqrt{9}/a$); (c) radiated power due to the uniform Josephson current for both the even and odd modes; and radiated power due to the cavity mode source for the (d) even and (e) odd modes.
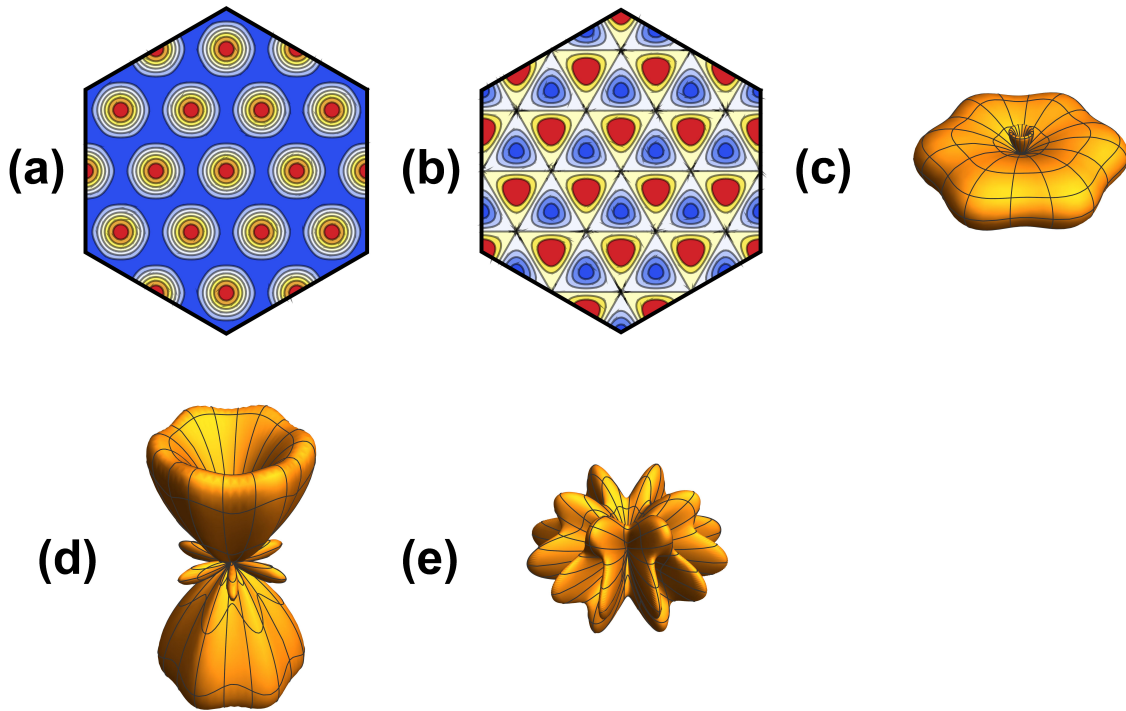

Figure B.6: (a) Contour plot of the wavefunction for the even TM(2,2) mode ($k_{22} \propto \sqrt{12}/a$); (b) radiated power due to the uniform Josephson current; and (c) radiated power due to the cavity mode source for the even mode.

Figure B.7: Contour plots of the wavefunctions for the (a) even and (b) odd TM(3,1) modes ($k_{31} \propto \sqrt{13}/a$); (c) radiated power due to the uniform Josephson current for both the even and odd modes; and radiated power due to the cavity mode source for the (d) even and (e) odd modes.
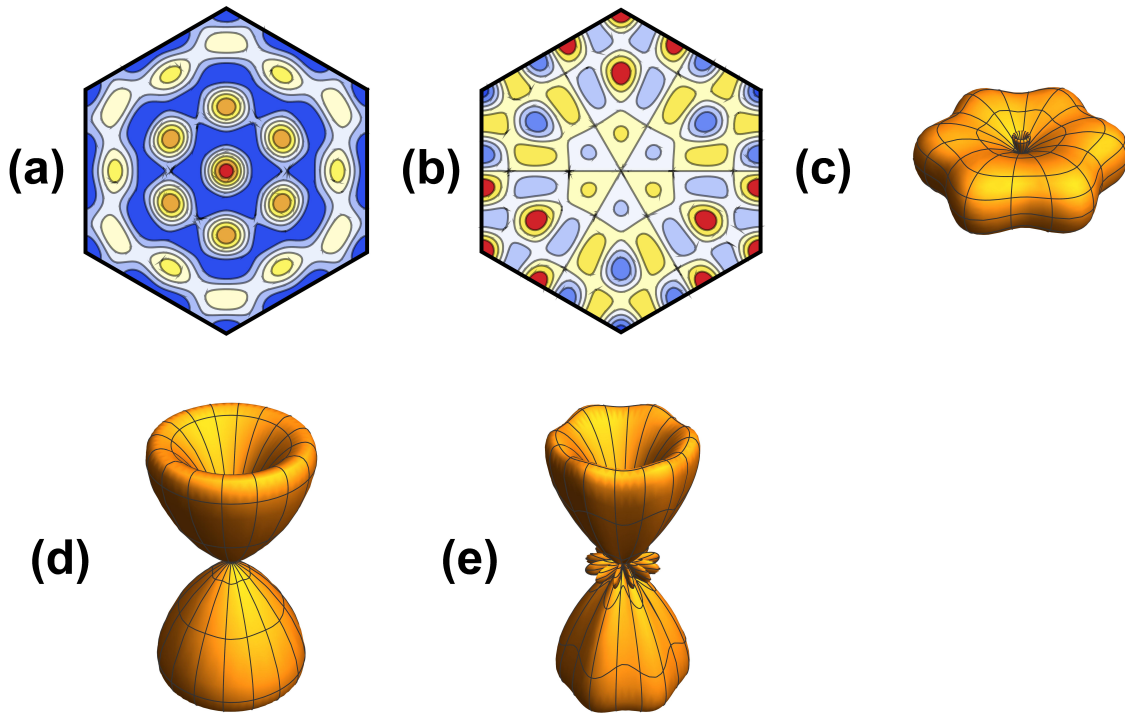
Figure B.8: Contour plots of the wavefunctions for the (a) even and (b) odd TM(4,0) modes ($k_{40} \propto \sqrt{16}/a$); (c) radiated power due to the uniform Josephson current for both the even and odd modes; and radiated power due to the cavity mode source for the (d) even and (e) odd modes.

Figure B.9: Contour plots of the wavefunctions for the (a) even and (b) odd TM(3,2) modes ($k_{32} \propto \sqrt{19}/a$); (c) radiated power due to the uniform Josephson current for both the even and odd modes; and radiated power due to the cavity mode source for the (d) even and (e) odd modes.
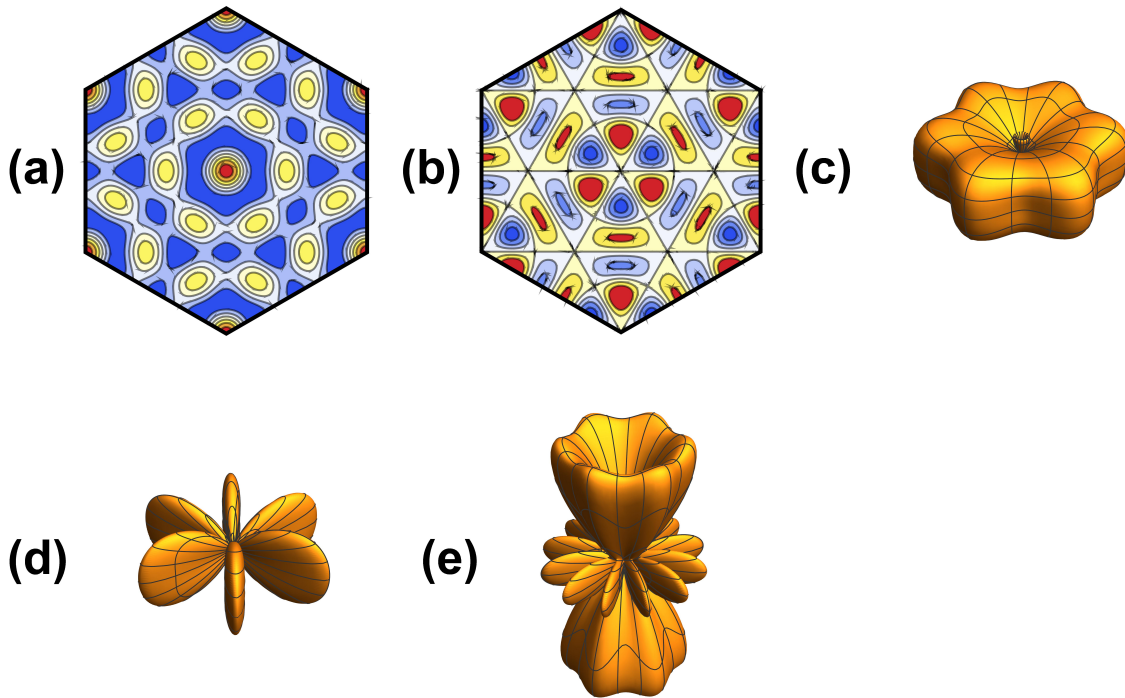
Figure B.10: Contour plots of the wavefunctions for the (a) even and (b) odd TM(4,1) modes ($k_{41} \propto \sqrt{21}/a$); (c) radiated power due to the uniform Josephson current for both the even and odd modes; and radiated power due to the cavity mode source for the (d) even and (e) odd modes.
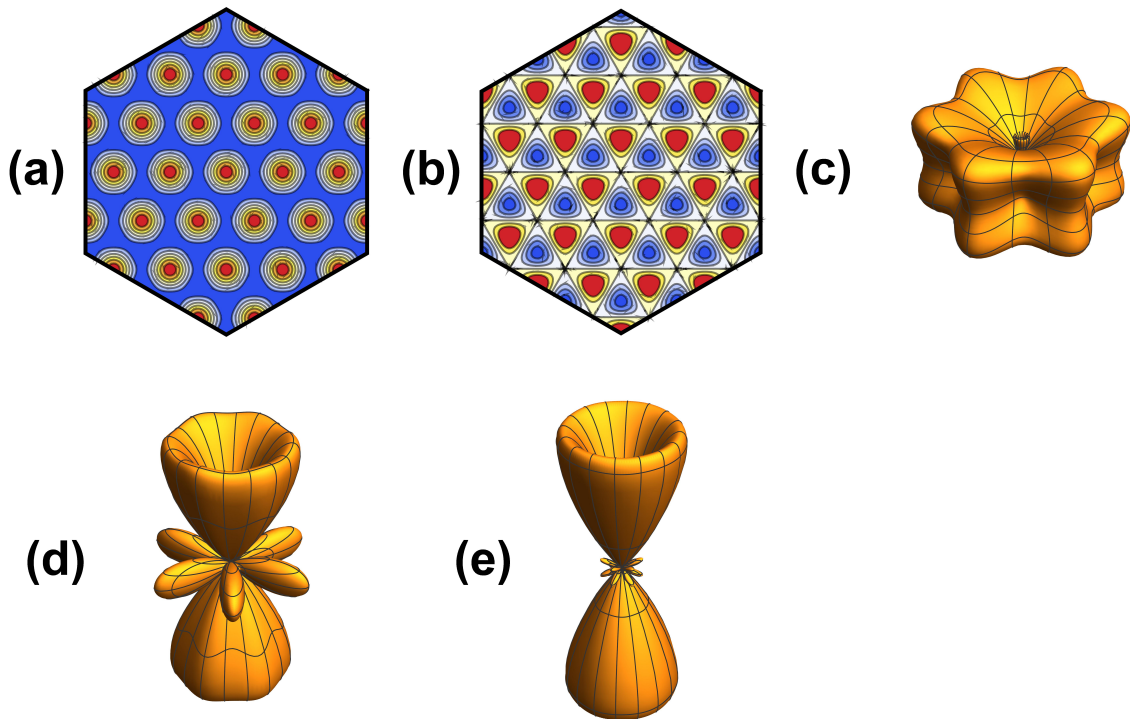
Figure B.11: Contour plots of the wavefunctions for the (a) even and (b) odd TM(5,0) modes ($k_{50} \propto \sqrt{25}/a$); (c) radiated power due to the uniform Josephson current for both the even and odd modes; and radiated power due to the cavity mode source for the (d) even and (e) odd modes.
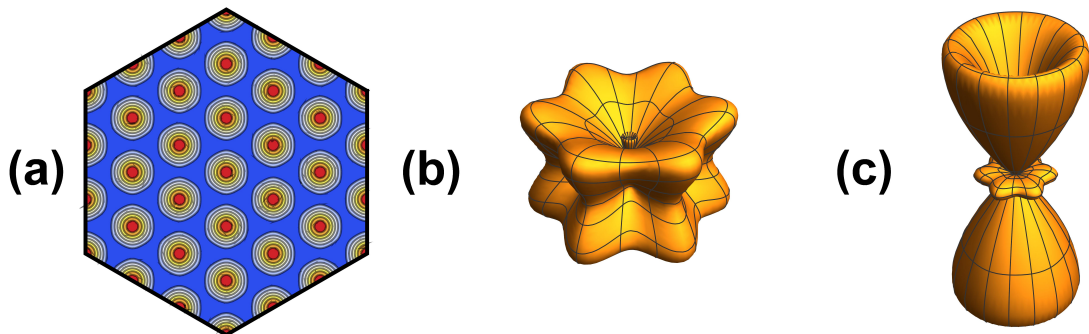

Figure B.12: (a) Contour plot of the wavefunction for the even TM(3,3) mode ($k_{33} \propto \sqrt{27}/a$); (b) radiated power due to the uniform Josephson current; and (c) radiated power due to the cavity mode source for the even mode.
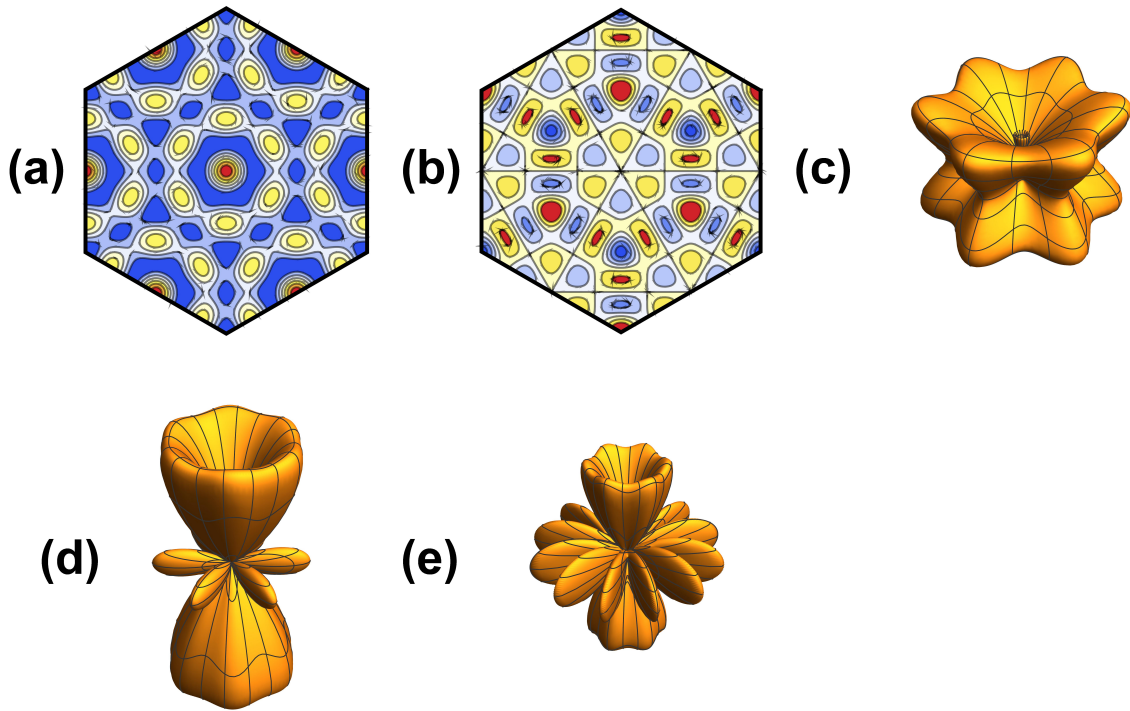
Figure B.13: Contour plots of the wavefunctions for the (a) even and (b) odd TM(4,2) modes ($k_{42} \propto \sqrt{28}/a$); (c) radiated power due to the uniform Josephson current for both the even and odd modes; and radiated power due to the cavity mode source for the (d) even and (e) odd modes.
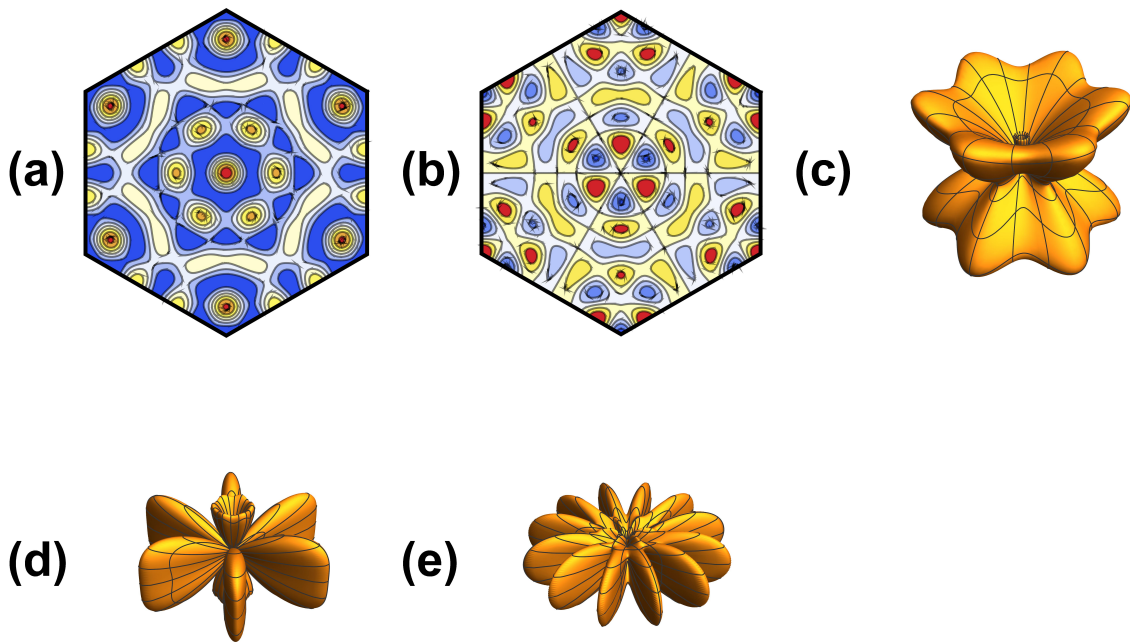
Figure B.14: Contour plots of the wavefunctions for the (a) even and (b) odd TM(5,1) modes ($k_{51} \propto \sqrt{31}/a$); (c) radiated power due to the uniform Josephson current for both the even and odd modes; and radiated power due to the cavity mode source for the (d) even and (e) odd modes.

Figure B.15: Contour plots of the wavefunctions for the (a) even and (b) odd TM(6,0) modes ($k_{60} \propto \sqrt{36}/a$); (c) radiated power due to the uniform Josephson current for both the even and odd modes; and radiated power due to the cavity mode source for the (d) even and (e) odd modes.
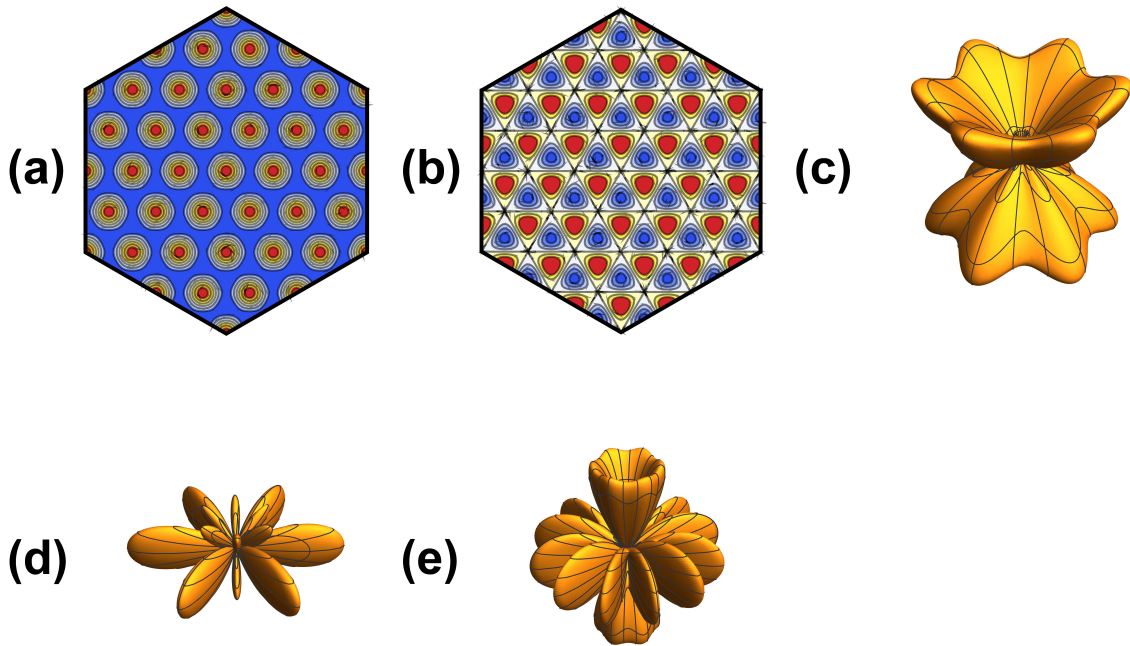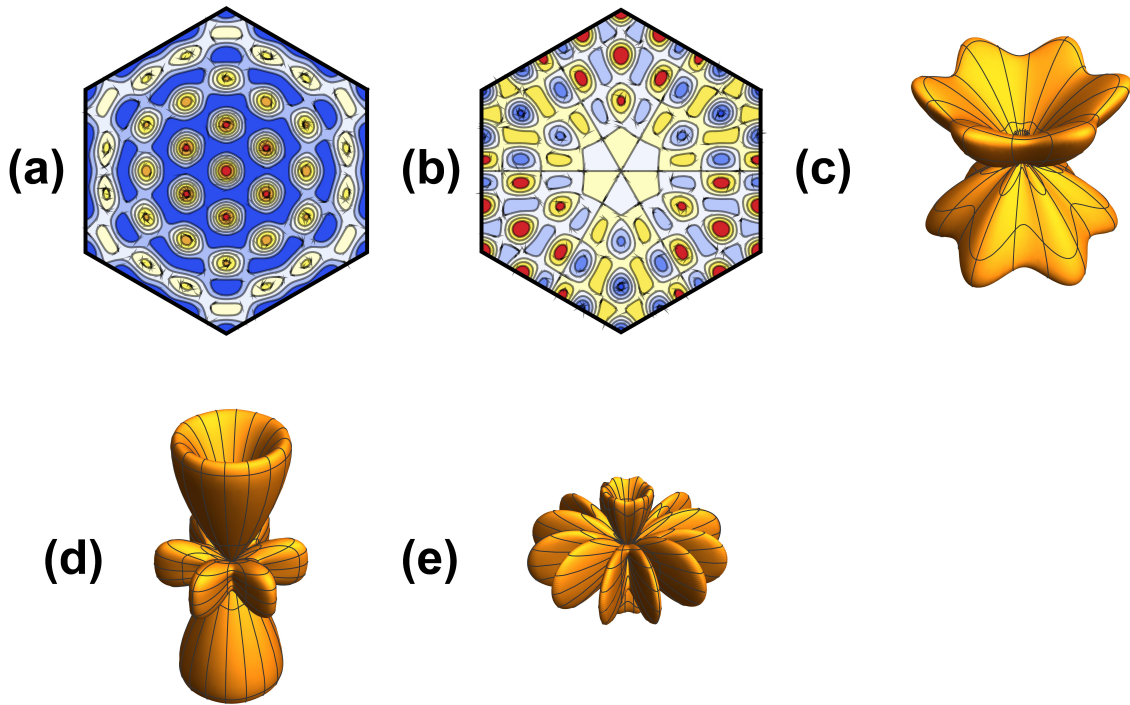
Figure B.16: Contour plots of the wavefunctions for the (a) even and (b) odd TM(4,3) modes ($k_{43} \propto \sqrt{37}/a$); (c) radiated power due to the uniform Josephson current for both the even and odd modes; and radiated power due to the cavity mode source for the (d) even and (e) odd modes.

LIST OF REFERENCES

[1] Welp U, Kadowaki K, and Kleiner R 2013, *Nature Photon.* **7** 702-710

[2] Suzuki S, Shiraishi M, and Shibayama H 2013, *J. Sel. Top. Quant. Electron.* **19** 8500108

[3] Williams B S 2007, *Nature Photon.* **1** 517-525

[4] Dobroiu A, Otani C, and Kawasi K 2006, *Meas. Sci. Technol.* **17** R161-R174

[5] Josephson B D 1962, *Phys. Lett.* **1** 251-253

[6] Kleiner R, Steinmeyer F, Kunkel G, and M uller P 1992, *Phys. Rev. Lett.* **68** 2394

[7] Klemm R and Kadowaki K 2010, *J. Phys.: Condens. Matter* **22** 375701

[8] Kashiwagi T, Yamamoto T, Minami H, Tsujimoto M, Yoshizaki R, Delfanazari K, Kitamura T, Watanabe C, Nakade K, Yasui T, Asanuma K, Saiwai Y, Shibano Y, Enomoto T, Kubo H, Sakamoto K, Katsuragawa T, Marković B, Mirković J, Klemm R A, and Kadowaki K 2015, *Phys. Rev. Appl.* **4** 054018

[9] Ozyuzer L, Koshelev A E, Kurter C, Gopalsami N, Li Q, Tachiki M, Kadowaki K, Yamamoto T, Minami H, Yamaguchi H, Tachiki T, Gray K E, Kwok W K, and Welp U 2007, *Science* **381** 1291-1293

[10] Bulaevskii L N and Koshelev A E 2006, *J. Supercond. Novel Magn.* **19** 349

[11] Kadowaki K, Tsujimoto M, Yamaki K, Yamamoto T, Kashiwagi T, Minami H, Tachiki M, and Klemm R A 2010, *J. Phys. Soc. Japan* **79** 023703

[12] Balanis C A 2005, *Antenna Theory, Analysis and Design* 3rd edn (Hoboken, NJ: Wiley)

[13] Tsujimoto M, Yamaki K, Yamamoto T, Kashiwagi T, Minami H, Tachiki M, and Klemm R A 2010, *Phys. Rev. Lett.* **105** 037005

[14] Klemm R A, Delfanazari K, Tsujimoto M, Kashiwagi T, Kitamura T, Yamamoto T, Sawamura M, Ishida K, Hattori T, and Kadowaki K 2013, *Physica C* **491** 30

[15] Klemm R A, Davis A E, Wang Q X 2017, *IEEE J. Sel. Top. Quantum Electron.* **23** 8501208

[16] Hu X and Lin S 2009, *Phys. Rev. B* **80** 064516

[17] Jones R S 2004, *Solutions of the two-dimensional Helmholtz equation.*

[18] Lamé G 1833, *Journal de l'Ecole Polytechnique* **22** 194-215

[19] Tinkham M 1964, *Group Theory and Quantum Mechanics* (McGraw-Hill)

[20] Fassetta S and Sibille A 2003, *IEE Proceedings* **150** 7569720